DYNAMICS OF LARGE-SCALE VORTICES IN NON-SWIRLING AND SWIRLING TURBULENT JETS. TIME-RESOLVED TOMOGRAPHIC PIV MEASUREMENTS

Vladimir M. Dulin

Kutateladze Institute of Thermophysics
Siberian Branch of the Russian Academy of Sciences
1 Lavrentyev Ave., Novosibirsk, Russia
vmd@itp.nsc.ru

Sergey S. Abdurakipov

Department of Physics
Novosibirsk State University
2 Pirogova Str., Novosibirsk, Russia
s.s.abdurakipov@gmail.com

Dmitriy M. Markovich

Kutateladze Institute of Thermophysics
Siberian Branch of the Russian Academy of Sciences
1 Lavrentyev Ave., Novosibirsk, Russia
dmark@itp.nsc.ru

Kemal Hanjalić

Faculty of Applied Science
Delft University of Technology
Julianalaan 136, 2628 BL Delft, The Netherlands

ABSTRACT

The paper reports on a parallel study of the dynamics of large-scale vortical structures in non-swirling, low-swirl and high-swirl turbulent jets by means of the time-resolved tomographic PIV technique. 3D realizations of the instantaneous velocity and velocity gradients, local strain and rotation rates, helicity and pressure fluctuations are analyzed. Deformation of the large-scale vortices is studied by evaluating the local stretching/compression rates and local values of the Lamb vector divergence. Linear stability analysis is also applied to the mean velocity profiles in order to identify the most unstable azimuthal modes.

INTRODUCTION

Large-scale vortex structures dominate the dynamics of momentum and scalar transport in the initial region of circular jet flows, but smaller-scale longitudinal vortices play an important role in mixing and, in particular, for stabilization of fuel-rich flames (Liepmann and Gharib, 1992; Demaire and Baillot, 2001). Besides, dynamics of large-scale vortices and their interactions have impact on acoustic noise emitted by jets. When swirl is imposed onto the jet, it promotes helical instability modes (Alekseenko et al., 2007), which start to dominate over ring-like vortices (Gallaire et al., 2004). Further increase of the swirl rate results in destabilization of the jet's swirling vortex core and its eventual breakdown (Billant et al., 1998; Sarpkaya, 1979). Bubble-type or cone-type recirculation zones occur in high-swirl jets after breakdown of the vortex core (Sarpkaya, 1979; Spall, 1996; Billant et al., 1998).

As concluded by Ruith et al. (2003), formation of the central recirculation zone triggers growth of a global (self-exciting) helical instability mode of the swirling jet's core (Oberleithner et al., 2012). Properties of large-scale vortices in high-swirl jets are studied extensively with the aid of the conditional averaging technique (Cala et al., 2006). However, less energetic helical vortices in low-swirl turbulent jets are studied in less details.

The present paper reports on the time-resolved tomographic PIV measurements of flow dynamics in turbulent non-swirling, low- and high-swirl jets and detailed analysis of the measured three-dimensional instantaneous velocity and velocity gradient distributions.

EXPERIMENTAL SETUP AND DATA PROCESSING

The swirling jet flow was organized in a closed hydrodynamic circuit, which included a water tank, pump, flowmeter, and test section. The rectangular test section ($200\times600\times200$ mm^3) was made of Plexiglas. A contraction nozzle at the bottom of the test section produced the jet flow. The nozzle exit diameter d was 15 mm. A vane swirler was mounted inside the nozzle to organize jets with swirl. Details on the nozzle and mean velocity data can be found in Markovich et al. (2016).

Using swirlers with different inclination angle of the blades, the geometrical swirl rate S defined by (1) was 0.41 and 1.0. These swirl rates are referred to as low and high swirl rates, respectively. According to the previous studies, a bubble-type central recirculation zone was present for the latter flow case, whereas no recirculation was observed in the mean velocity field for the former case. The vortex core precession took place for both cases of S, but for the low-swirl jet it was less energetic and was not associated with a distinct precession frequency.

$$S = \frac{2}{3}\left(\frac{1-\left(d_1/d_2\right)^3}{1-\left(d_1/d_2\right)^2}\right)\tan\left(\psi\right) \qquad (1)$$

Here, $d_1 = 7$ mm is the diameter of the centre body, supporting the blades, $d_2 = 27$ mm is the external diameter of the swirler, and ψ is the inclination angle of the blades. The Reynolds number $\mathrm{Re} = U_0 d/\nu$ is based on the bulk jet velocity U_0 and water kinematic viscosity ν.

The measurement volume of $40\times40\times40$ mm^3 (approximately $2.5d\times2.5d\times2.5d$) was recorded by four high-speed CMOS cameras (Photron FASTCAM SA5). Polyamide seeding particles

(50 μm in size) in the measurement volume were illuminated by a high-repetition pulsed Nd:YAG laser (Photonix DM100-532) with the average power of 100 W. The illumination area was organized as a vertical cylindrical beam of 40 mm in diameter.

The in-house "ActualFlow" software, developed in the Institute of Thermophysics, was used to measure and process the acquired images. The cameras and laser were synchronized by a BNC 575 device from Berkeley Nucleonics. The acquisition frequency was 2 kHz. During each run, 2000 images were recorded. Three independent runs were carried out for each swirl case to verify the consistency of the results for a single run. The cameras were calibrated by capturing images of a plane target (150×150 mm^2), moved through the measurement volume by a microscrew traverse. A self-calibration procedure (similar to that of Wieneke, 2008) was used prior to the tomographic reconstruction of the 3D images. The final average disparity after correction was less than 0.07 pixels, whereas the uncorrected disparity was up to 10 pixels.

The tomographic reconstruction of 3D images was carried out by the conventional two-frame technique MLOS + 15 SMART (Atkinson and Soria, 2009). The size of the reconstructed 3D images was $571\times571\times571$ voxels. The 3D field of the particle displacement was evaluated by using a 3D multi-frame pyramid correlation algorithm (similar to that of Sciacchitano et al., 2012) with a pyramid base of 3 images. Local spatial correlation between the images was calculated by an iterative multi-grid algorithm with continuous interrogation volume shift and deformation (Scarano, 2002). The final size (Δ) of the interrogation domains, where each particles velocity vector was evaluated, was $3.36\times3.36\times3.36$ mm^3 ($48\times48\times48$ voxels). The spatial grid-overlapping factor was set to 75%. Thus, the distance between the neighbouring vectors was 0.84 mm.

To minimize the contribution of random error to the velocity derivatives, the instantaneous velocity fields were post-processed by temporal and spatial filters before calculating the velocity gradient. Each velocity vector was individually smoothed over time via a sliding average filter with the kernel of 10 time steps, which is equivalent to low-pass filter with a cut-off frequency of 200 Hz. The cut-off frequency was selected based on the sampling frequency and the ratio between the maximum displacement of all particles and Δ. Thereafter, the velocity vectors were smoothed by 3D spatial Gaussian filter with FWHM of approximately 1.3 mm (≈18 voxels)

DATA ANALYSIS

Quantitative analysis of the vortices deformation is based on the rates of the vortex stretching/compression and tilting (Violato and Scarano, 2011) in the equation (2), where $\boldsymbol{\omega} = \nabla \times \mathbf{u}$ is the instantaneous vorticity.

$$|SR| = \left| (\boldsymbol{\omega}\nabla)\mathbf{u} \cdot \frac{\boldsymbol{\omega}}{|\boldsymbol{\omega}|} \right|, \quad |TR| = \left| (\boldsymbol{\omega}\nabla)\mathbf{u} \times \frac{\boldsymbol{\omega}}{|\boldsymbol{\omega}|} \right| \qquad (2)$$

Divergence (3) of the Lamb vector $\mathbf{l} = \boldsymbol{\omega}\times\mathbf{u}$ (Hamman et al. 2008) is analysed to reveal regions, where the local "flexion product" exceeds enstrophy. Thus regions with positive $\nabla\mathbf{l}$ indicate conversion of the angular to linear momentum (i.e., unwinding of vortex structures and depletion of the low pressure zone, see Hanjalić, and Mullyadzhanov, 2015).

$$\nabla\mathbf{l} = \left(\mathbf{u}\cdot\left[\nabla\times\boldsymbol{\omega}\right]\right) - \left(\boldsymbol{\omega}\boldsymbol{\omega}\right) \qquad (3)$$

Besides, local pressure fluctuations (at the scales resolved by PIV) are evaluated based on the 3D PIV data and Navier-Stokes equations (see van Oudheusden et al., 2013). This is done by solving a modified Poisson equation with Smagorinsky model for effective viscosity $\nu_{eff} = (C_S\Delta)^2|S_{ij}|$, often used in large-eddy simulations (Sagaut, 2006), and by neglecting the effect of molecular viscosity for the turbulent incompressible flow:

$$\Delta p = -\rho\nabla\left(\left(\mathbf{u}\nabla\right)\mathbf{u} - \nabla\left(\nu_{eff}\mathbf{S}\right)\right) \qquad (4)$$

S_{ij} is the strain rate tensor of the velocity; C_S is constant taken to be equal to 0.1. The numerical solution of the Poisson equation is performed by a second-order accurate in-house solver, utilizing the Gauss-Seidel method.

Besides, a linear stability analysis is applied for the time-averaged data in a similar manner to Oberleithner et al. (2011). Although the linear stability analysis relies on the conditions of small velocity perturbations (and moreover, the time-averaged velocity is not a solution of the Navier-Stokes equations) this method can be useful for prediction of the most unstable modes in turbulent flows.

The principles rely on the triple decomposition of the instantaneous velocity field (and pressure) (Hussain and Reynolds, 1970):

$$\mathbf{u} = \mathbf{U} + \mathbf{u}' = \mathbf{U} + \langle\mathbf{u}\rangle + \mathbf{u}'', \qquad (5)$$

where $\mathbf{U} = \langle\mathbf{u}\rangle$ is the time-averaged velocity field, $\langle\mathbf{u}\rangle$ and $\mathbf{u}''$ are the components of the velocity fluctuations associated with coherent flow motions and the residual broadband stochastic ("background") turbulence, respectively. The former component is defined via a certain conditional sampling technique (in case of quasi-periodic fluctuations of the flow it is performed via phase-averaging). Equation for the coherent component $\langle\mathbf{u}\rangle$ can be obtained from the Naiver-Stokes equations and continuity equation:

$$\frac{\partial\langle\mathbf{u}\rangle}{\partial t} + \langle\mathbf{u}\rangle\nabla\mathbf{U} + \mathbf{U}\cdot\nabla\langle\mathbf{u}\rangle = -\frac{1}{\rho}\nabla\langle p\rangle + \nu\nabla^2\langle\mathbf{u}\rangle - \nabla\boldsymbol{\tau}, \quad \nabla\langle\mathbf{u}\rangle = 0 \qquad (6)$$

Equation (6) also relies on the negligibility of non-linear terms of $\langle\mathbf{u}\rangle\mathbf{u}''$. The components of the stress tensor $\boldsymbol{\tau}$ contain information about the momentum exchange between the mean (time-averaged), coherent (phase-averaged) and residual components of the velocity. The stress tensor is modeled via a linear eddy viscosity model, which results in the linear differential equations for $\langle\mathbf{u}\rangle$.

$$\boldsymbol{\tau} = \nu_t\mathbf{S}, \text{ where } \nu_t = -\left\langle u_r'u_y'\right\rangle \Big/ \left(\frac{\partial U_y}{\partial r} + \frac{\partial U_r}{\partial y}\right) \qquad (7)$$

The local linear stability framework under quasi-parallel assumption of the mean flow is used to provide valuable information about frequency and wavelength of the most unstable modes. The coherent velocity and pressure field $q = \{u, p\}$ is decomposed into the normal modes with respect to axial and azimuthal homogeneous directions:

$$q(r,\theta,y,t) = \hat{q}(r)\exp\left(i(ky + m\theta - \omega t)\right) + c.c\,, \qquad (8)$$

where $k = k_{re} + ik_{im}$ corresponds to the complex streamwise wavenumber, ω is the angular frequency, and m is the number of the azimuthal mode. The azimuthal angle θ increases in the direction of the jet swirl.

The solution of the equations (6-8) with appropriate boundary conditions provides the dispersion relation $k = k(\omega)$ for complex-valued k and real-valued ω. A well-established Chebyshev pseudospectral collocation technique is used to discretize and solve the obtained eigenvalue problem (see Khorrami et al., 1989; Oberleithner et al., 2011). The performance of the algorithm is verified against the data from LES simulations of non-swirl pipe jet in Mullyadzhanov et. al. (2016) and also against the data of other authors.

RESULTS

Stability analysis

The main purpose of the spatial stability analysis of swirling jets in this paper was to obtain additional information on the spiral modes observed in the experiment. Spatial stability analysis of swirling jet was carried out for a sequence of mean velocity profiles in 20 different axial positions (the 2D data of time-resolved 2D PIV measurements of an air jet flow with Re = 5000 is reported in Alekseenko et al., 2012). The axial and azimuthal components of the mean velocity were approximated correspondingly by the analytical expressions used by Gallaire and Chomaz (2006) and later by Oberleithner et al. (2014) for the low-swirl jet and by the expressions from Oberleithner et al. (2011) for the high-swirl jet with central recirculation zone.

In case of the low-swirl jet, it was possible to identify two physical eigenvalues with positive growth rates. One type of eigenvalues was assigned as shear instability modes, whereas the others were associated with centrifugal instability modes (of the jet core). The shear modes we found to exist in the absence of the swirl (when the azimuthal velocity was set to zero), whereas the centrifugal modes were present only in the presence of swirl.

Figure 1 shows the dispersion curves of the spatial stability analysis for axial position $y/d = 0.2$ near the nozzle exit. $R_{0.5}$ is the radial coordinate of the axial shear layer and U_C is the centerline velocity. Magnitude of the growth rate of the shear instability modes is significantly higher than that of the centrifugal mode. This circumstance allowed to distinguish them between each other during the analysis. Figure 3 shows the most unstable modes for different cross-sections.

It is found that for small distances from the nozzle (y/d less than 0.5) the axisymmetric mode $m = 0$ has the highest growth rate. Downstream, the analysis predicts the highest growth for mode $m = 1$. Growth rates of the centrifugal instability modes are sufficiently smaller in comparison to the shear instability modes. The most unstable centrifugal modes are $m = -2$ and -1, which winded in the same direction as the jet swirl (i.e., $k_{re} > 0$).

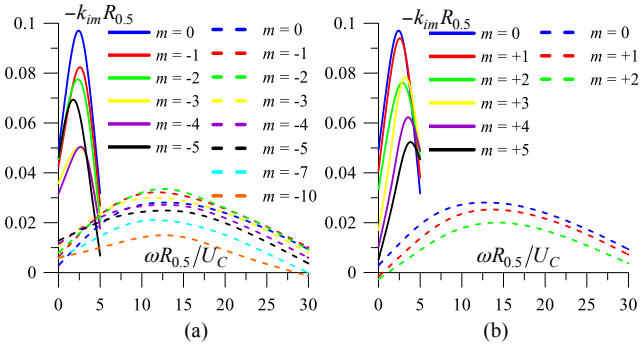

Figure 1. Dispersion curves of the most unstable modes for a low-swirl jet for $y/d = 0.2$. Shear layer (solid lines) and centrifugal (dashed lines) modes

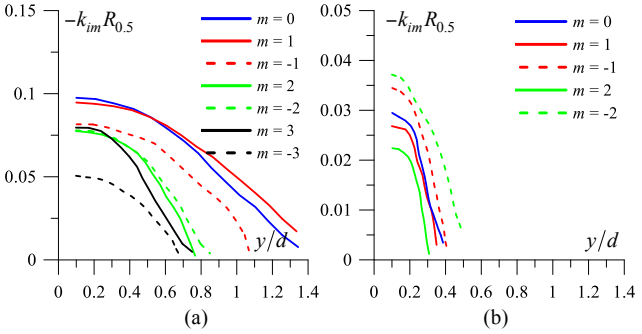

Figure 2. Dependence of the growth rate of the most unstable modes for a low-swirl jet for different y/d. (a) Shear layer and (b) centrifugal modes

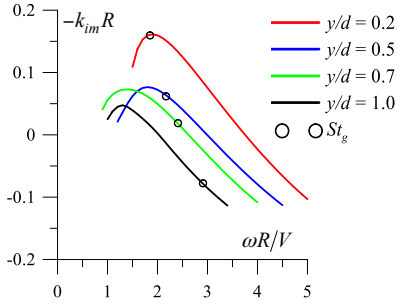

Figure 3. Dispersion curves for the most unstable mode $m = +1$ for a high-swirl jet for different y/d

Dispersion curves for the most unstable mode $m = +1$ for the high-swirl jet are shown in Figure 4 for different cross-sections ($y/d = 0.2$, 0.5, 0.7, 1.0). For each cross-section, terms of the equation (6) are normalized by the maximum value of the axial velocity and $V = U_{y,\max}$ and the corresponding radius $R = r_{y,\max}$. The rest modes are not discussed because their growth rates are significantly lower. The range of $\omega R/V$ values, where mode $m = +1$ is unstable, decreases downstream. For the distances

downstream $y/d = 0.76$ azimuthal mode $m = +1$ becomes stable for any frequency.

3D data

The time-averaged velocity data measured previously by Alekseenko et al. (2008) by using stereoscopic 2D PIV is plotted in Figure 4 (Re = 8900). The axial velocity reaches negative values for the case $S = 1.0$ and corresponds to the presence of central recirculation zone. Figure 5 shows the comparison of the 2D and 3D data for the high-swirl jet with vortex breakdown. The profiles manifest reasonable correspondence.

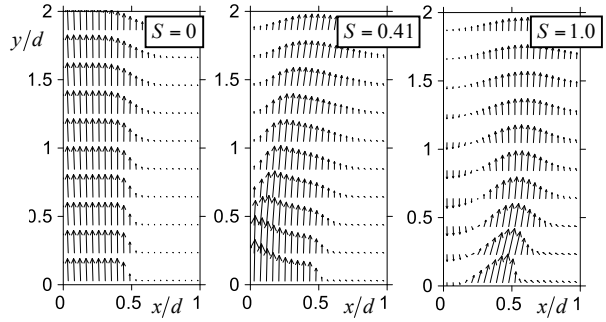

Figure 4. Time-average velocity data from 2D PIV data

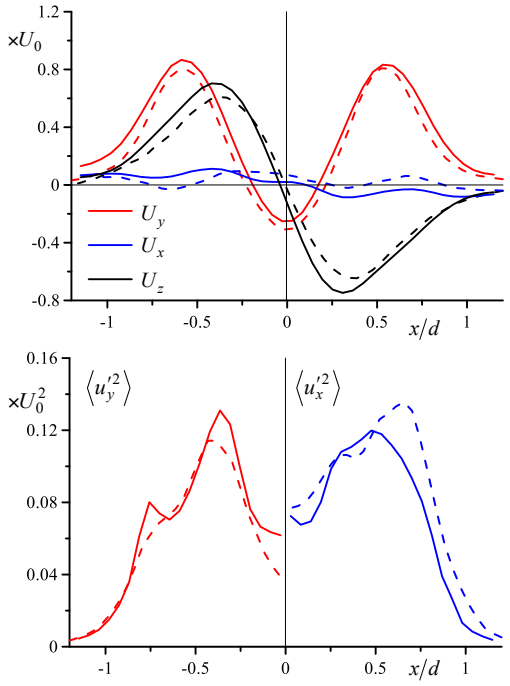

Figure 5. Comparison of time-averaged 2D (solid lines) and 3D (dashed lines) PIV data for the high-swirl jet

Large-scale vortices in the instantaneous velocity snapshots in Figure 6b are visualized by Q-criterion (Hunt et al., 1988). The ring-like vortex structure (RV) is also shown in Figure 6a by semi-transparent gray iso-surfaces of $Q = 0.5U_0^2/d^2$. One can observe that deformation of RV occurs under interaction with longitudinal vortex filaments (red and blue surfaces).

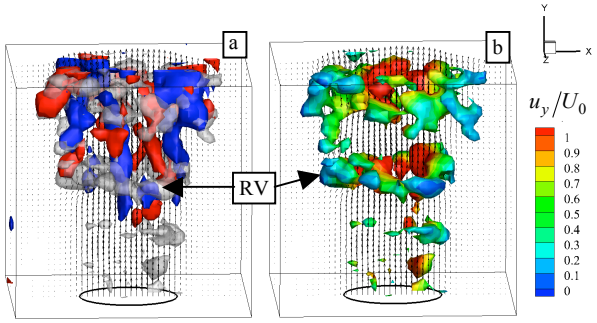

Figure 6. Vortex structures in a non-swirling jet. (a): blue and red regions correspond to the axial vorticity $< -1U_0/d$ and $> +1U_0/d$, respectively. (b) Large-scale vortices are visualised by Q-criterion ($> 0.5U_0^2/d^2$)

The time-averaged values of the Lamb vector divergence of and rate of vortices stretching are shown in Figures 7a and 7b, respectively. The former plot visualizes local regions for the mixing layer with linear momentum increase and decrease, associated with vortical fluid motion. SR reaches highest values in the mixing layer of the jet, where ring-like vortices are being tilted, deformed and stretched.

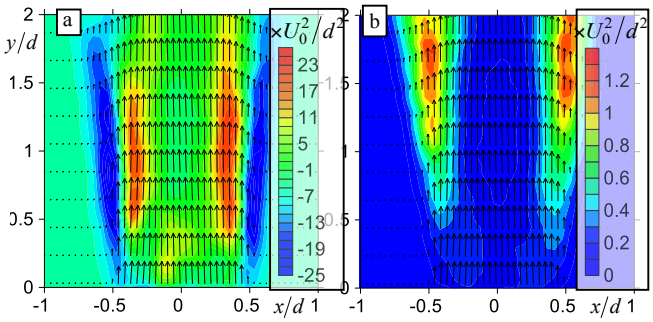

Figure 7. Time-averaged values of the (a) Lamb vector divergence and (b) rate of vortices stretching for a non-swirling jet

The example of the instantaneous velocity snapshot in the low-swirl jet with visualization of the large-scale vortices is shown in Figure 8. Figures 8a and 8b show iso-surfaces for the local helicity and pressure. Extensive region with positive helicity correspond to the swirling jet, whereas regions with negative helicity are induced in the outer mixing layer between the jet and surrounding fluid. Iso-surfaces for the local pressure value of $-0.2\rho U_0^2/2$ are coloured according to the local axial velocity. The lowest pressure values are found in the swirling jet core.

Figures 8c and 8d visualize large-scale vortex structures by iso-surfaces of Q-criterion. The iso-surfaces are colored according to the local values of helicity and divergence of the Lamb vector. The large-scale vortex structure around the jet axis is the swirling jet's vortex core (VC), corresponding to positive values of the local helicity. This structure is surrounded by a region of positive Lamb vector divergence. However, the spatial distribution of the averaged values of the Lamb vector divergence, shown in Figure 9a, reveals negative values around the jet axis (inside the axial large-scale vortex structure).

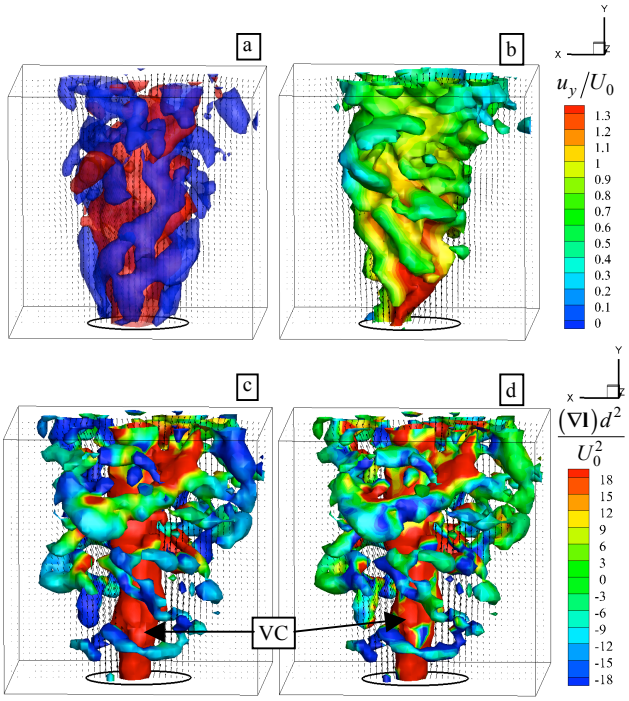

Figure 8. Vortex structures in a low-swirl jet. (a): blue and red regions correspond to the local helicity $< -0.5U_0^2/d$ and $> +2U_0^2/d$, respectively. (b) pressure iso-surfaces ($-0.2\rho U_0^2/2$) coloured according to the local axial velocity. Large-scale vortices are visualised by Q-criterion ($> 0.4U_0^2/d^2$) and coloured according to the local (c) helicity and (d) lamb vector divergence

The averaged values of |ST| are shown in Figure 9. The maximum rates of vorticity stretching correspond to the jet core and are associated with axial velocity decrease downstream the nozzle exit. Thus, expansion of the swirling jet downstream the nozzle exit provides decrease of the linear momentum around the jet axis.

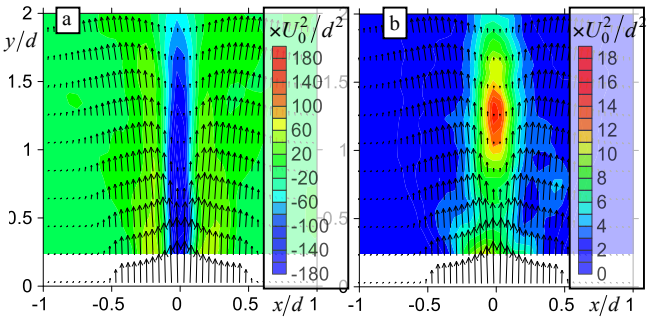

Figure 9. Time-averaged values of the (a) Lamb vector divergence of the (b) rate of vortices stretching for a low-swirl jet

The example of the instantaneous velocity snapshot for the high-swirl jet is shown in Figure 10. Regions with positive and negative helicity are shown in Figure 10a. Figure 10b plots iso-surface with regions of local pressure of $-0.4\rho U_0^2/2$. The lowest pressure is detected inside the recirculation zone. Q-criterion is used in Figures 10c and 10d to visualize the large-scale vortex structures. The flow of the high-swirl jet is more turbulent. Despite this, a long helical vortex can be distinguished in the outer mixing layer from the other smaller vortical structures. Local color of the surfaces in Figure 10c correspond to the local helicity and visualizes that the reverse flow around the jet axis results in an extensive region with negative local helicity.

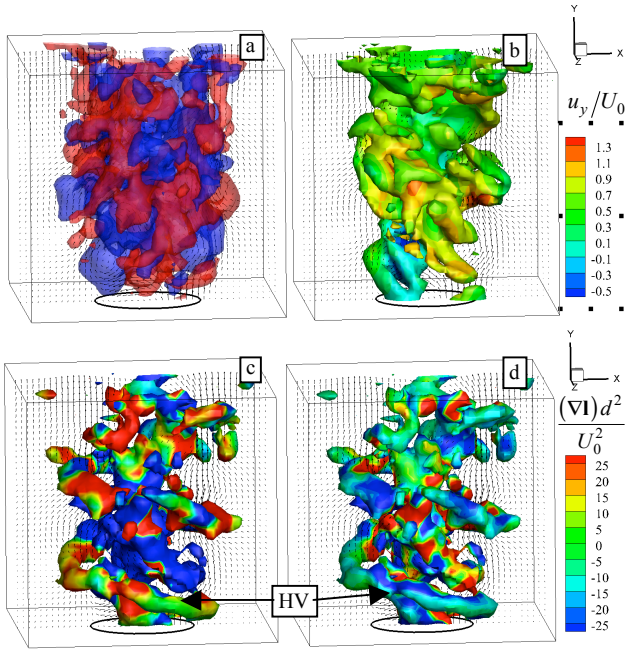

Figure 10. Vortex structures in a high-swirl jet. (a): blue and red regions correspond to the local helicity $< -0.7U_0^2/d$ and $> +0.7U_0^2/d$, respectively. (b)) pressure iso-surfaces ($-0.4\rho U_0^2/2$) coloured according to the local axial velocity. Large-scale vortices are visualised by Q-criterion ($> 1.5U_0^2/d^2$) and coloured according to the local (c) helicity and (d) lamb vector divergence

The average Lamb vector divergence and rate of vortices stretching are shown in Figure 11a and 11b, respectively. The stretching rate reaches maximal values around the central recirculation zone. As in the case of low-swirl jet, the average Lamb vector divergence is negative around the jet core. The annular jet core is associated with positive values of the divergence, probably due to local linear momentum increase compensating negative axial velocity in the reverse flow.

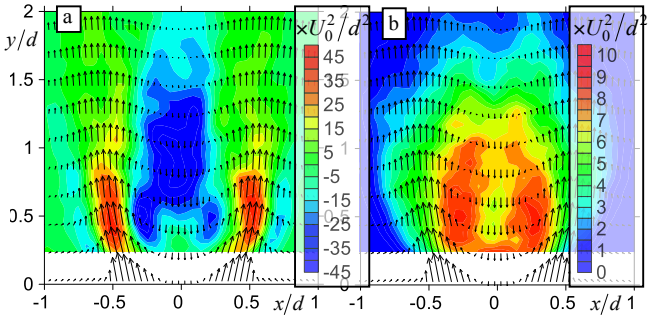

Figure 11. Time-averaged values of the (a) Lamb vector divergence and (b) rate of vortices stretching for a high-swirl jet

CONCLUSIONS

Flow dynamics of turbulent non-swirling, low-swirl and high-swirl jets have been studied by time-resolved tomographic PIV measurements. Deformations of large-scale vortex structures have been quantified by analyzing the three-dimensional instantaneous velocity and velocity gradient fields. Linear stability analysis, based on a linear eddy viscosity model, was also applied for the mean velocity distributions.

Near the nozzle exit of the non-swirling and low-swirl jets, the analysis predicted the highest growth rate for the axisymmetric mode $m = 0$. Downstream $y/d = 0.5$, growth rate of the azimuthal mode $m = +1$ for the low-swirl jet became higher than that for the mode $m = 0$. Modes $m = -2$ and -1 were found to be most unstable for the core region of the low-swirl jet. Toroidal vortices were also detected in 3D PIV data for the mixing layer of the non-swirling and low-swirl jets. In the latter case they broke apart and formed longitudinal vortex filaments. Core of the low-swirl flow was featured by a local decrease of the axial momentum due to the expansion of the swirling jet.

The high-swirl jet was featured by a bubble-type vortex breakdown with central recirculation zone. The stability analysis predicted helical mode $m = +1$ (counter-winding to the direction of the jet swirl) to be the most unstable. Similar structure was found in the 3D velocity snapshots in the outer mixing layer.

ACKNOWLEDGEMENTS

The authors are grateful to Dr. M.Hrebtov for the pressure evaluation algorithm. This research was supported by grants of the President of the Russian Federation.

REFERENCES

Alekseenko, S.V., Kuibin, P.A., and Okulov, V.L., 2007, *Theory of concentrated vortices: an introduction*, Springer Science & Business Media

Alekseenko, S.V., Dulin, V.M., Kozorezov, Y.S., and Markovich, D.M., 2008, "Effect of axisymmetric forcing on the structure of a swirling turbulent jet", *International Journal of Heat and Fluid Flow*, Vol. 29, pp. 1699-1715

Alekseenko, S.V., Chikishev, L.M., Dulin, V.M., and Markovich, D.M., 2012, "Study of vortex breakdown in swirling premixed flames by high-repetition stereoscopic PIV", *Proceedings, 7th International Symposium on Turbulence, Heat and Mass Transfer*, Palermo, Italy

Atkinson, C., Soria, J., 2009, "An efficient simultaneous reconstruction technique for tomographic particle image velocimetry", Experiments in Fluids, Vol. 47, pp. 553-568

Billant, P., Chomaz, J.-M., and Huerre, P., 1998 "Experimental study of vortex breakdown in swirling jets", *Journal of Fluid Mechanics*, Vol. 376, pp. 183-219

Cala, C.E., Fernandes, E., Heitor, M.V., and Shtork, S.I., 2006, "Coherent structures in unsteady swirling jet flow", *Experiments in Fluids*, Vol. 40, pp. 267-276

Gallaire, F., Rott, S., and Chomaz, J.M., 2004. "Experimental study of a free and forced swirling jet", *Physics of Fluids*, Vol. 16, pp. 2907-2917

Gallaire, F., and Chomaz, J.M. 2003 "Mode selection in swirling jet experiments: a linear stability analysis" *Journal of Fluid Mechanics*, Vol. 494, pp. 223-253

Hamman, C.W., Klewicki, J.C., and Kirby, R.M., 2008, "On the Lamb vector divergence in Navier–Stokes flows", *Journal of Fluid Mechanics,* Vol. 610, pp.261-284

Hanjalić, K., Mullyadzhanov, R., 2015, "On spatial segregation of vortices and pressure eddies in a confined slot jet", *Physics of Fluids*, Vol. 27, 031703

Hunt, J.C.R., Wray, A.A., and Moin, P., 1988 "Eddies, stream, and convergence zones in turbulent flows". *Proceedings, 8th Summer Program, Center for Turbulence Research. S*tanford Univ., CA8

Hussain, A.K.M.F., and Reynolds, W.C., 1970, "The mechanics of an organized wave in turbulent shear flow", *Journal of Fluid Mechanics*, Vol. 41, pp. 241-258

Khorrami, M.R., Malik, M.R., and Ash, R.L., 1989, "Application of spectral collocation techniques to the stability of swirling flows", *Journal of Computational Physics*, Vol. 81, pp. 206-229

Liepmann, D., and Gharib, M., 1992, "The role of streamwise vorticity in the near-field entrainment of round jets", *Journal of Fluid Mechanics*, Vol. 245, pp. 643-668

Markovich, D.M., Dulin, V.M., Abdurakipov, S.S., Kozinkin, L.A., Tokarev, M.P., and Hanjalic, K., 2016, "Helical modes in low- and high-swirl jets measured by tomographic PIV" *Journal of Turbulence*, Vol.17, pp. 678-698

Mullyadzhanov, R., Abdurakipov, S., and Hanjalić, K., 2016. "Helical structures in the near field of a turbulent pipe jet", *Flow, Turbulence and Combustion*, Vol. 981, pp. 367-388

Oberleithner, K., Sieber, M., Nayeri, C.N., Paschereit, C.O., Petz, C., Hege, H.C., and Wygnanski, I., 2011, "Three-dimensional coherent structures in a swirling jet undergoing vortex breakdown: stability analysis and empirical mode construction", *Journal of Fluid Mechanics*, Vol. 679, pp. 383-414

Oberleithner, K., Paschereit, C.O., Seele, R., and Wygnanski, I., 2012, "Formation of turbulent vortex breakdown: intermittency, criticality, and global instability", *AIAA Journal*, Vol. 50, pp. 1437-1452

Oberleithner, K., Paschereit, C.O., and Wygnanski, I., 2014, "On the impact of swirl on the growth of coherent structures", *Journal of Fluid Mechanics*, Vol. 741, pp. 156-199

Ruith, M.R., Chen, P., Meiburg, E., and Maxworthy, T., 2003, "Three-dimensional vortex breakdown in swirling jets and wakes: direct numerical simulation", *Journal of Fluid Mechanics*, Vol. 486, pp. 331-378

Sagaut, P., 2006, *Large eddy simulation for incompressible flows: an introduction*. Springer Science & Business Media

Sarpkaya, T., 1979, "Vortex-induced oscillations: a selective review", *Journal of Applied Mechanics*, Vol. 46, pp. 241-258

Scarano, F., 2002, "Iterative image deformation methods in PIV", *Measurement Science and Technology*, Vol. 13, R1

Sciacchitano, A., Scarano, F., and Wieneke, B., 2012. "Multi-frame pyramid correlation for time-resolved PIV", *Experiments in Fluids*, Vol. 53, pp. 1087-1105

Spall, R.E., 1996, "Transition from spiral-to bubble-type vortex breakdown", *Physics of Fluids*, Vol. 8, pp. 1330-1332

van Oudheusden, B.W., 2013, "PIV-based pressure measurement", *Measurement Science and Technology*, Vol. 24, 032001

Violato, D., and Scarano, F., 2011, "Three-dimensional evolution of flow structures in transitional circular and chevron jets", *Physics of Fluids*, Vol. 23, 12410

Wieneke, B., 2008, "Volume self-calibration for 3D particle image velocimetry", *Experiments in Fluids*, Vol. 45, pp. 549-556